HYPERFINE MAPPING OF DONOR WAVE FUNCTION DEFORMATIONS IN SILICON PHOSPHORUS BASED QUANTUM DEVICES

A Thesis

Submitted to the Faculty

of

Purdue University

by

Seung Hyun Park

In Partial Fulfillment of the

Requirements for the Degree

of

Master of Science in Electrical and Computer Engineering

December 2009

Purdue University

West Lafayette, Indiana

This thesis is dedicated to my parents.

ACKNOWLEDGMENTS

I would like to thank my advisor, Professor Gerhard Klimeck who gave me the opportunity to work on researches with valuable insights and all the required resources since the beginning of my graduate year. I also thank to my co-advisor, Professor Lloyd C. L. Hollenberg for providing novel ideas and the opportunities to work on researches and the significant scientific guidance. I also like to thank all the members of Klimeck group for countless discussions. Special thanks to Dr. Rajib Rahman who shows me the way of what I should pursue as a researcher, and he guided me as my mentor and as my best friend. I was really fortunate to work with him. I thank to Neerav Kharche and Seokmin Hong for the countless scientific discussions. I am also grateful for discussions with Mathieu Luisier, Benjamin Haley, Samarth Agawal, Abhijeet Paul, Muhammad Usman, Amritanshu Palaria, Hoon Ryu, Sunhee Lee, Saumitra Mehrotra, Sung Geun Kim, Ganesh Hegde, Prijat Sengupta, Yaohua Tan, Xufeng Wang, Matthias Tan, Woo-Suhl Cho, and Zhengping Jiang. I am also grateful for the interactions with Professor Sven Rogge, Dr. Andrew Greentree, Dr. Chris Escott, and Daniel Drumm. I appreciate the valuable input from my other committee member, Professor Datta who leads me to this area through his lecture 'Fundamentals of Nanoelectronics' in my undergraduate at Purdue University.

The project was supported by the Australian Research Council, the Australian Government, and the U.S. National Security Agency (NSA), Advanced Research and Development Activity (ARDA), and the Army Research Office (ARO) under Contract No. W911NF-08-1-0527. Part of this work was done at JPL, Caltech under a contract with NASA. NCN/nanohub.org computational resources were used.

TABLE OF CONTENTS

Page

LIST OF TABLES v

LIST OF FIGURES vi

ABSTRACT vii

1. INTRODUCTION: IMPURITIES IN NANOSTRUCTURES 1

2. SINGLE DONOR PHYSICS AND MODELING FOR HYPERFINE CALCULATION 4

2.1 Basic Single Donor Physics and Modeling 4
2.2 Hyperfine Coupling Modeling 5

3. HYPERFINE MAPPING DONOR WAVE FUNCTION DEFORMATIONS AT SUB-BOHR ORBIT RESOLUTION 8
3.1 Abstract 8
3.2 Introduction 8
3.3 Methodology: Hyperfine Interaction Calculation and Method (NEMO 3-D) 10
3.4 Results 12
3.4.1 Concept of Shell 12
3.4.2 Practical Implementation of the Experiment 13
3.4.3 Calculation of Hyperfine and Anistotropic Hyperfine Frequency Peak .. 16
3.5 Conclusion 19

4. FUTURE WORK: QUANTUM TRANSPORT THROUGH SINGLE DONOR IN A SHORT CHANNEL SEMICONDUCTOR 20

LIST OF REFERENCES 22

A. CONCEPTS AND FIGURES OF SHELL 26
B. REFERENCE TABLES FOR HYPERFINE CALCULATION 30

LIST OF TABLES

Table

Page

2.1 Comparison of the quadratic Stark coefficients from TBC experiment, EMT, BMB, and TB 6

3.1 Quadratic and linear Stark coefficients..... 17

B.1 Isotropic hyperfine and modulus of super hyperfine interactions (in Mhz) for group V donors in Si 30

B.2 Experimental results for hyperfine tensors in arsenic-, phosphorus-, and antimony dopred silicon 31

LIST OF FIGURES

Figure

Page

1.1 Bloch sphere 2

1.2 A schematic of B. E. Kane's quantum computing model 2

2.1 Schematic of a substitutional phosphorus donor impurity in a Si crystal 4

3.1 Schematic of the technique 10

3.2 Relative change in the contact hyperfine coupling 15

3.3 Stark shifted spectrum of a P donor at 3.8nm from an oxide interface 18

3.3 (a), (b), (c) The P donor ground state wave functioin at three different electric fields 18

3.3 (d), (e), (f) The corresponding hyperfine maps of (a) (b) (c) in the form of Byy tensor component 18

4.1 The schematic of a short channel semiconductor with single donor 20

A.1 Shells of the [001] axis class 26

A.2 Shells on the xy plane of (110) plane 27

A.3 Shells on the xz plane of (110) plane 27

A.4 Shells on the yz plane of (110) plane 28

A.5 Atom locations on two lines joining 4 corners of a cube 28

A.6 Atom locations on two lines joining 4 corners of a cube 29

ABSTRACT

Park, Seung Hyun M.S.E.C.E., Purdue University, December 2009. Hyperfine Mapping of Donor Wave Function Deformations in Si:P based Quantum Devices. Major Professors: Gerhard Klimeck and Lloyd C. L. Hollenberg.

The exponential miniaturization of semiconductor technology over the past 50 years has ushered in an era of nano-scale quantum electronics. As device sizes are shrinking, discrete dopant based Si nanostructures are expected to play a vital role in future electronics, and are the subject of much current research due to its scalibility and coherence time. However, there is still lack of direct knowledge how the electronic wave functions vary for different structures and how they can be engineered by electric and magnetic fields.

We investigated how to map out donor electron wave function deformations in single donor system. To investigate single donor physics relevant to quantum architecture we used the Nano Electronic Modeling Tool (NEMO 3D) which provides semi-empirical tight-binding model using sp3d5s* models with or without spin to treat several million atoms. In the work, we studied a method for mapping the subtle changes that occur in the electron wave function through the measurement of the full hyperfine tensor probed by silicon isotope (29Si) in the presence of perturbations. Our results showed that detecting the donor wave function deformation is possible at sub-Bohr radius level.

The accomplishment of 3-D mapping of electron with perturbations would aid in designing, engineering and manufacturing nanoscale devices, as well as next-generation microchips and other electronics with nanoscale features. It also might be useful in advancing quantum computing. Moreover, the technique has potential for wide applicability. In principle, it could be used to map wavefunctions in single electron silicon quantum dots, quantum wells and other nanostructures of interest.

1. INTRODUCTION: IMPURITIES IN NANOSTRUCTURES

Silicon-based quantum nanoelectronic systems represents the past expertise of the semiconductor industry in scalable system design and manufacture. However, at near atomic dimensions, conventional silicon device operations are strongly affected by quantum phenomena in the solid-state. A few number of impurities in the devices has affected on the quantum nanoelectronic systems stronger than previous era. For example, the few impurities in silicon nanosturtures are important factor due to interception in transistor.

However, there are advantages for using impurities in silicon nanostuructures. Analogously, impurities are considered as quantum dots at low temperature. Individual dopants capture electrons in their potential nest like quantum dots, and the dopants provide access to a number of quantum phenomena typically associated with single atoms. 3-D quantum confinement of electrons can be used for many applications such as spintronics and quantum computing architectures [1-3]. However, precisely duplicating same size of quantum dot is hard work in experiments. Instead of duplicating quantum dots, placing same kinds of donors such as phosphorus in silicon (Si:P) and arsenic in silicon (Si:As) takes advantages because of their identical potential of impurities. There are recent successful research results about placing impurities precisely [4-6].

One of the most important next generation applications is donor based quantum computing (QC) [1]. QC has one important difference compared to classical computing. Classical computing encode information based on a bit, and the bit information is composed of ‘zero’ state ($|0\rangle$) or ‘one’ state ($|1\rangle$). However, quantum bit or qubit of quantum computer can record information both in the ‘zero’ and ‘one’ states simultaneously as a superposition ($A\,|0\rangle + B\,|1\rangle$). This two level quantum mechanical system of quantum computer can be represented geometrically by Block sphere.

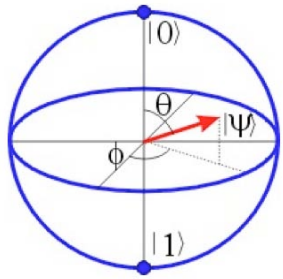

Figure 1.1 Bloch sphere geometrically represents of two spinors / quantum states (A |0> + B |1>) in terms of points on a unit sphere. (*note: A and B are complex numbers, and the states have to be normalized, and $|A|^2 + |B|^2 = 1$)

This novel way of the encoding information leads a quantum computing device to a next generation computing model. Silicon-based quantum systems take an advantage of long spin coherence times for stable qubit control. As a result there are a number of key proposals for quantum computing including substitutional donors [1, 7-9], gate-confined 2DEGS [10], and Si quantum wells [11]. In particular, the initial research thrust provided by Kane's donor qubit proposal [1] have led to a number of important experiments on gate control of a single donors [4-6]. The system based on P donors nuclear spin and electron spin in silicon encodes information by transferring electron spin stored P nuclear spin information near interface via gate control.

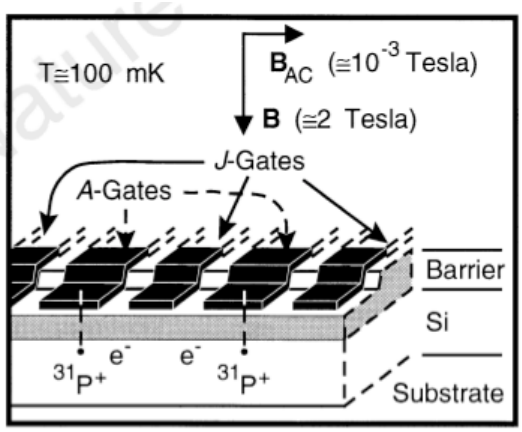

'A silicon-based nuclear spin quantum computer' Kane, Nature (1998)

Figure 1.2 Illustration of two cells in a one-dimensional array containing 31 P donors and electrons in a Si host, separated by a barrier from metal gates on the surface.

Hyperfine interaction between the donor electron spin and nuclear spin is the main key for precise donor qubit control in the above system. Another important interaction is the exchange coupling to the two adjacent qubits. To treat hyperfine and exchange interaction there are J gate and A gate. First, A gate is placed above the donor, and it can vary the hyperfine interaction. Second, J gate is located in the between two donors to modulate the exchange coupling, and control the overlap of two electronic wave function.

Our research focuses on the electronic structure of few P impurities in silicon for nanoelectronic and quantum computing applications. The impurity wave functions typically span for several nano meters in the crystal, giving rise to the possibility of exercising gate control in the above kinds of systems. Our primary focus is to investigate quantum control of such impurities for high fidelity qubit design. Specifically, in this report we investigated hyperfine interaction in the Si:P based nanoelectronic system. The theoretical model is based on tight-binding methods to treat multiple problems in the atomistic scale. Even though there is the effective mass models, by using tight -binding model we can consider Bloch state in the host material. It can treat strain and perturbations such as magnetic fields and electric fields. Hence, for this study we employed semi-empirical tight-binding theory under the hood of the Nanoelectronic Modeling Tool (NEMO 3D) [12]. NEMO 3D has been successfully applied to compute Stark shift of the donor contact hyperfine coupling in excellent agreement with experiments and with momentum space methods. The method was also used to interpret single donor transport experiments in FinFETs [13].

Thesis body is composed of three chapters. In chapter 2, we present basic donor physics in silicon and semi-empirical method for impurity modeling in tight-binding model. We also describe basic concept of hyperfine coupling in Si:P, and modeling method and technique [16] in chapter 2. In chapter 3, we present a method to map donor wave functions indirectly and directly with perturbation by hyperfine interaction. As explained above for Kane's QC model [1] the hyperfine interaction is a critical issue to control donor wave function by field perturbations in the impurity quantum dots precisely due to the high sensitivity of qubit control in the quantum devices. Yet, it is not well understood how the electronic wave functions vary in the dopant based silicon nanostructures and how they can be engineered precisely by electric and magnetic fields. We investigated the feasibility of measuring the field-induced deformation in the donor wave functions [20]. In chapter 4, we describe our future plan for Si:P based device simply.

2. SINGLE DONOR PHYSICS AND MODELING TOWARDS HYPERFINE INTERACTION CALCULATION

2.1 Basic Single Donor Physics and Modeling

Since our research focuses on the electronic structure properties of single donor physics, we describe the physical system and modeling method in this chapter. Impurities which can supply additional electrons to the conduction band are so-called electron donors. In the case of P substitutional impurity (group V) in silicon (group IV), The P ion has charge 5e and contributes five valence electrons, and the 4 electrons from the outside of closed shell of P donor are bonding with the 4 neighboring Si atoms. The additional positive charge of P donor is located at its site, and an additional electron is along with the charge at low temperature in the potential of P donor. The additional electron is ionized to the conduction band at moderate temperature.

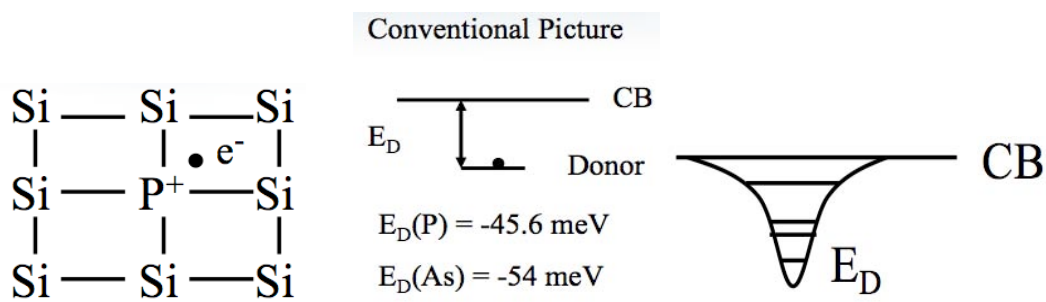

Figure 2.1 Left: Schematic representation of a substitutional phosphorus donor impurity in a Si crystal. Middle: Phosphorus donor effect in conduction band of semiconductor. Right: Phosphorus potential generates quantum dot like hole at low temperature.

The Si:P system form a Hydrogen-like system which has six fold degeneracy corresponding to the valley structure of the silicon conduction band. The system has valley orbit interaction due to deviations of the impurity potential from its coulombic nature in the vicinity of the donor nucleus. In 1950s, Kohn and Luttineger studied

theoretical donor spectrum for the electrons bound by P, As, or Sb donors by effective mass theory (EMT) [14-15]. They took account into account the fact that the conduction band of Si has six equivalent minima. Their method is still employed by a lot of scientists who study quantum devices based on Si:P, but people start recognizing the demands of more accurate model which take care of more extended set of Bloch states in recent research. To carry out precise modeling of Si:P system, Rahman et al employed two sophisticated methods such as semiempirical tight-binding method and Band Minima Basis (BMB) to investigate Stark tuning of donor spins in Si:P system in the presence of interfaces with effect of core of donor and valley orbit splitting and added into the account to model impurities [16] by using NEMO 3-D [16].

The theoretical model matches with experimental results well, and was derived the Stark effect for various depths. This modeling method was applied to various topics such as coherent tunneling via adiabatic passage (CTAP) [17], gate induced g-factor control [18], and charge qubit control [19] for Si:P based quantum computing modeling under the guidance of professor G. Kimeck and professor L. C. L. Hollenberg. Parts of the method and modeling technique are used for 'High precision quantum control of single donor spins in Si' [16] to do 'Mapping donor electron wave function deformations at sub-Bohr orbit resolution' [20], and the technique is well-described in chapter 3.

2.2 Hyperfine Coupling Modeling

In this subsection, we describe the modeling of hyperfine interaction based on Rahman et al.'s approaches [16]. The spin Hamiltonian of donor electron with field applied perturbations such as an electric field $\vec{E}$ and a magetic field B_0 is, $H_Z = g(\vec{E})\mu_B B_0 S_Z + A(\vec{E}) I_Z S_Z$, where $A(\vec{E})$ and $g(\vec{E})$ are the hyperfine coupling constant and electron g-factor. The hyperfine coupling '$A(\vec{E})$' is proportional to coupling strength between donor nuclear and spin of electron wave function in our Si:P system, and that means this coupling is proportional to $\left|\Psi(\vec{E},\vec{r_0})\right|^2$ where r_0 corresponds to the coordinates of the impurity site. The potential of impurity site is added into the calculation as,

$$V(\vec{r}) = \frac{e}{4\pi k\left|\vec{r}-\vec{r_0}\right|}, \vec{r} \neq \vec{r}_0 , \tag{2.1}$$

$$V(\vec{r}) = U_0, \vec{r} = \vec{r}_0 \tag{2.2}$$

The above concept lead us to the idea of possibility of measuring electron wave function from the hyperfine coupling. In the work, we extract coefficients of quadratic Stark effect for the bulk case. It shows that far from interface quadratic Stark effect dominates, but interface regime linear Stark effect can be comparable to quadratic Stark effect. The change of Stark effect leads the change of $A(\vec{E})$, and it can be expressed as,

$$\frac{\Delta A(\vec{E})}{A(0)} = \eta_2 E^2 + \eta_1 E\,, \tag{2.3}$$

$$\frac{\Delta A(\vec{E})}{A(0)} = \frac{\left|\Psi(\vec{E},\vec{r_0})\right|^2}{\left|\Psi(0,\vec{r_0})\right|^2} \tag{2.4}$$

There is novelty of the method and technique. By using tight-binding model we can consider Bloch state in the host material, and it can treat strain and perturbations much better than EMT. Also, the results matches well with experiments compared to EMT. Even though tight-binding model consumes much more computation source, the preciseness is the demand of the next novel devices like Si:P based quantum computing device. The advantages can be checked in the below table.

Table 2.1 Comparison of the quadratic Stark coefficients from TBC experiment, EMT, BMB, and TB. In the above table, Experiment (Sb) result is taken from Ref [6], and the EMT result estimated from [21].
'High precision quantum control of single donor spins in Si'
R. Rahman et al, PRL 99, 036403 (2007)

Method	Depth (nm)	$\eta_2(\mu m^2/V^2)$
Experiment (Sb) [10]	150	-3.7×10^{-3}
EMT (P) [11]	∞	-2×10^{-2}
BMB (P)	10.86	-2.74×10^{-3}
TB (P)	10.86	-2.57×10^{-3}
	21.72	-2.76×10^{-3}

As mentioned in Introduction Chapter, Kane's donor based QC model [1] requires highly precise control of single donor spins, and by field perturbations control of the single qubit is possible. Hence, the hyperfine interaction between the donor electron spin and the nuclear spin of the P impurity is important factor to decide the precision of the control in this operation. Also, the donor wave function is proportional to hyperfine

coupling, and we could expect donor wave function distribution from hyperfine coupling calculation [20].

3. HYPERFINE MAPPING OF DONOR WAVE FUNCTION DEFORMATIONS AT SUB-BOHR ORBIT RESOLUTION

3.1 Abstract

Quantum wave function engineering of dopant–based Si nanostructures reveals new physics in the solid-state, and is expected to play a vital role in future nanoelectronics. Central to any fundamental understanding or application is the ability to accurately characterize the deformation of the electron wave functions in these atom-based structures through electric and magnetic field control. We present a method for mapping the subtle changes that occur in the electron wave function through the measurement of the hyperfine tensor probed by 29 Si impurities. We calculate Stark parameters for six shells around the donor. Our results show that detecting the donor electron wave function deformation is possible with resolution at the sub-Bohr radius level.

3.2 Introduction

The exponential miniaturization of semiconductor technology over the past 50 years has ushered in an era of nano-scale quantum electronics. At near atomic dimensions, conventional device operations are strongly affected by quantum phenomena in the solid state [13]. To ensure continued progress in semiconductor electronics, and indeed in the drive for new quantum nanoelectronic devices, the inherently quantum mechanical aspects of such systems need to be understood and even incorporated into device functionality. Furthermore, the exciting possibility of harnessing quantum phenomena in device has produced revolutionary ways of performing computing and electronic device operations, as exemplified by the rapidly developing fields of quantum computing and spintronics [1-3]. A central concept of quantum nanoelectronics is the ability to induce controlled deformation of a specific-magnetic fields. Accessing the details of such wave function engineering is critical to understanding and developing new

devices and applications. However, until now there has been no way of quantifying the type and nature of such wave function distortions beyond indirect means [13].

In this report, we propose an electron-nuclear double resonance (ENDOR) experiment to directly measure the gate induced Stark shift of the donor electron hyperfine tensor at specific lattice sites near the donor site (Figure 3.1). Individual 29 Si atoms at random in the lattice provide a direct nuclear spin probe of the donor electron wave function within the Bohr orbit region. Our large scale atomistic tight-binding simulations for large lattice regions involving over a million atoms, show that this technique provides a spatial map of the bound donor electron response to a controlling gate field to sub-Bohr orbit resolution, with excellent correlation to the spatial dependence of the deformed electronic wave function, and confirm the feasibility of detecting such field induced hyperfine resonance shifts. The technique has wide applicability as it can in principle be extended to map out electric field response of wave functions in single electron Si quantum dots, quantum wells or other nanostructure.

Silicon-based quantum nanoelectronic systems posses inherent advantages of long spin coherence times and vast expertise of the semiconductor industry in scalable system design and manufacture. As a result there are a number of key proposals for quantum computing devices, including substitutional donors [1, 2, 7-9], gate-confined 2DEGs [9], and Si quantum wells [11]. Advances in single atom [22] and ion implementation [23] technologies have opened the possibility of fabricating dopant based nanostructures in the laboratory in a repeatable manner. Some of the recent structures include a single gated donor in a FINFET [13], a gated two donor charge qubit [24], a 2D gated donor layer [4], and an 1D metallic wire of donors [5] between nanostructures vary considerably form their bulk counter parts, yet are critical to device operation. A direct map of the wave functions and their electric field response will be of enormous importance in novel quantum device design and engineering.

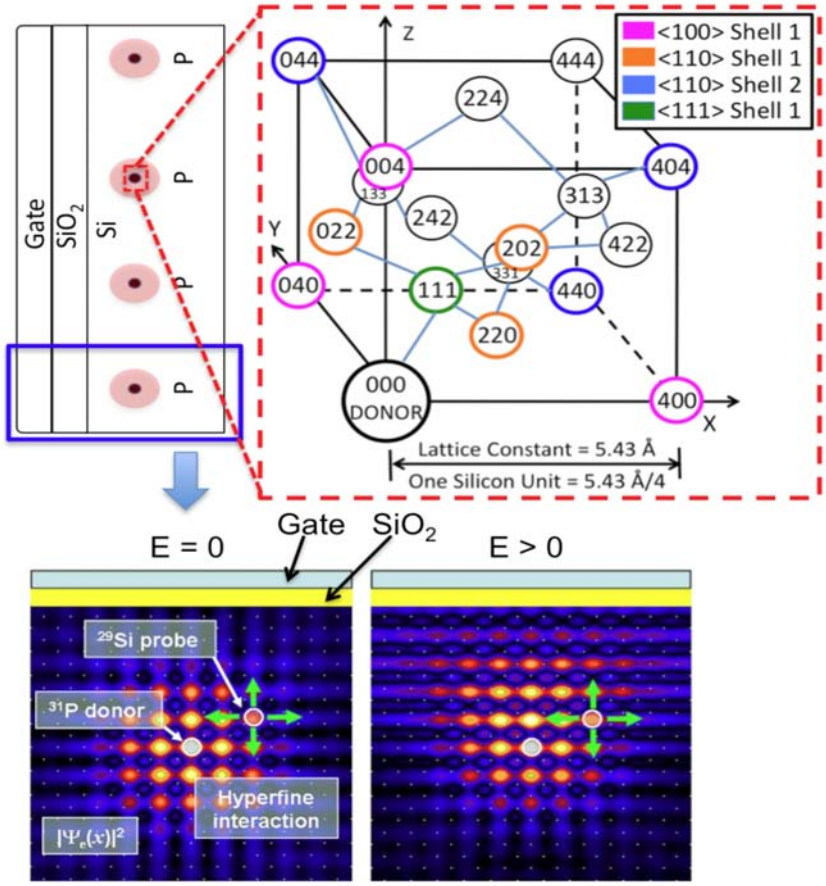

Figure 3.1 Schematic of the technique. Top row: A series of donors in Si under a gate. Inset shows classification of the sub-Bohr radii region into shells based on symmetry and distance. Bottom row: Probing the field-induced distortions of the donor wave function by a 29 Si atom using hyperfine interactions.

3.3 Methodology: Hyperfine interaction calculations and methods (NEMO 3D)

The method we describe here uses the hyperfine interaction between a donor electron spin and a nuclear spin of a 29 Si isotope in a lattice of spinless 28 Si atoms, the system originally measured by Hale and Mieher [27], but critically we include and analyze the effect of a controlling field deforming the donor wave function. Although current technology limits the substitution of a 28 Si atom by a 29 Si atom at a specific point in the lattice, it is nevertheless possible to prepare ensemble device samples (Figure 3.1) with 29 Si atoms distributed randomly around a gated donor. The hyperfine interaction between a donor electron spin S and a 29 Si nuclear spin I is $H = \vec{I} \cdot A \cdot \vec{S}$. Taking the origin at the 29 Si nucleus, the A tensor is

$$A_{ij} = \Upsilon_I \Upsilon_S \hbar^2 (\frac{8\pi}{3} |\psi(0)|^2 + \left\langle \psi \left| \frac{3r_i r_j - r^2 \delta_{ij}}{r^5} \right| \psi \right\rangle \tag{3.1}$$

where γ_I and γ_S are the nuclear and electronic gyromagnetic ratio respectively, and r_{ij} = (x, y, z). The first term in (1) is the Fermi contact hyperfine interaction, denoted here as β, and it directly proportional to the electronic probability density at the 29 Si site. The second term represents the magnetic dipolar or anisotropic hyperfine interaction between the two spins, denoted as B_{ij}. This dipolar them can also contribute to the ENDOR resonance energies providing a further measure of the distribution of the donor electron wave function about the provide site.

ENDOR measurements were performed, first by Feher [26] and later by Hale and Mieher [27], to study parts of the ground state wave function of a donor close to the nucleus, resolving as many as 20 shells (Figure 3.1) [27]. Several theoretical models have calculated the hyperfine tensors of a few shells with semi-quantitative agreement with the experiments [27, 28]. A recent ab-initio DFT study was able to calculate very accurately the tensor components of a few shells in the vicinity of the donor nucleus [29]. Changes in the Fermi contact hyperfine constants under a uni-directionally applied stress were also measured [30]. It was shown [31] that inclusion of the anisotropic hyperfine interaction in spin coherence time calculations provides remarkable agreement between theory and recent measurements. The only work on the Stark shift of the hyperfine tensors to date computed the Fermi contact coupling for 3 lattice sites [32].

The single donor wave functions subjected to constant electric fields were computed using an atomistic semi empirical tight-binding (TB) model involving a 20 orbital per atom basis of sp3d5s* (spin) orbitals with nearest neighbor interactions. The donor was modeled by a Coulomb potential with a cut-off value U0 at the donor site. The magnitude of U0 was adjusted to obtain the experimental binding energy of Si:P. The impurity potential is modeled as,

$$V(\vec{r}) = \frac{e}{4\pi k \left| \vec{r} - \vec{r_0} \right|}, \vec{r} \neq \vec{r}_0 , \tag{3.2}$$

$$V(\vec{r}) = U_0, \vec{r} = \vec{r}_0 \tag{3.3}$$

*note: k is the dielectric constant of Si, assuming a value of 11.9 ε_0

The total Hamiltonian was diagonalized by a parallel Lanczos eigensolver to obtain the low lying impurity wave functions, which were then used to evaluate the hyperfine tensors using equation (1). The TB method used here is embedded in the Nanoelectronic Modeling Tool (NEMO 3D) [12], and has been successfully applied to compute Stark shift of the donor contact hyperfine coupling [16] in excellent agreement with experiments [6] and with momentum space methods [33]. The method was also used to interpret single donor transport experiments in FinFETs [13].

3.4 Results

3.4.1 Concept of shell

From the perspective of an experimentalist, one of the most difficult aspects of this experiment is to identify which 29 Si site is responsible for a particular hyperfine peak. In previous experiments, lattice sites were grouped into shells and symmetry classes to mark data analysis easier. In accordance with previous works, we use a coordinate system centered on the donor site, and denote lattice sites about the donor by 3 integers (n1, n2, n3) with the distance measured in units of $a_0/4$. For an unperturbed lattice, a shell is the group of lattice sites equidistant from the donor, whose hyperfine tensors for one member of the shell, it is possible to obtain the tensors of all the points in the shell from symmetry arguments. A shell can further be grouped into one of four symmetry classes.

The <001> axis class contains all points (n1, n2, n3) such that two of these integers are zero. A particular shell of this class has 6 lattice sites with coordinates $\{(m,0,0),(\overline{m},0,0),(0,m,0),(0,\overline{m},0),(0,0,m),(0,0,\overline{m})\}$, where m is a positive integer in multiples of 4. The <111> axis class contains all points with $|n1|=|n2|=|n3|\neq 0$ and has 4 members per shell. For example, the 4 nearest neighbors of the donor impurity form a shell of the <111> axis class. The {110} plane class comprise all sites with two out of the three integers equal in magnitude and non-zero. Each shell has 12 members and consists of the points $\{(m,m,n),(m,\overline{m},n),(\overline{m},m,n),(\overline{m},\overline{m},n),(m,n,n),(m,n,\overline{m}),(\overline{m},m,m),$ $(\overline{m},n,\overline{m}),(n,m,m),(n,m,\overline{m}),(n,\overline{m},m),(n,\overline{m},\overline{m})\}$. The 4th class is called the unique class and contains all points with $|n1|\neq|n2|\neq|n3|$. The first shell of this class is quite far away

from the donor and is not resolve in experiments. Even with precise theoretical model, it can be difficult in practice to resolve shells a few lattice units away from the donor. (*note: Appendix A - Concepts and figures of shell)

3.4.2 Practical implementation of the experiment

Two major issues need to be addressed for practical implementation of the experiments. First, it is necessary to associate each hyperfine resonance peak with a 29 Si lattice site. Second, electrostatic gates may give rise to inhomogeneous electric fields in the lattice, subjecting each donor to a different Electric field, and may limit the distinguishability of signals corresponding to a 29 Si site.

The First issue has been resolved in previous works by classifying the lattice sites according to their symmetry and distance from the donor. For example, the lattice sites in the [100] equivalent directions from the donor are grouped into a different symmetry class as opposed to the points in the [110] or [111] directions. At E=0, all the points equidistant from the donor are responsible for a single hyperfine peak, and can be grouped as a shell for ease of identification. At a non-zero Electric field, these points are no longer equivalent, giving rise to multiple resonance peaks. As an example, there are 6 points one lattice constant a_0 away from the donor along the [100] equivalent directions. If an Electric field directed along [010] is applied, the four points (with lattice sites $(\pm a_0,0,0)$ and $(0,0,\pm a_0)$) lying in a plane perpendicular to the field are still equivalent, and produce a single resonance peak. Since the site $(0,a_0,0)$ is at a different potential than $(0,-a_0,0)$, two separate peaks are observed. Overall, the six-fold degenerate hyperfine peak splits into 3 components (Fig 3.2a).

To minimize the effect of inhomogeneous Electric fields, it is usually advantageous to introduce the donors by ion implementation rather than by bulk doping. Ion implementation at several 100 keVs with typical doses of $10^{11} cm^{-2}$ can ensure a rapidly decaying Gaussian depth distribution with a sharply peaked mean depth [6, 34]. Several such implementation doses introduced laterally along the surface give rise to a fairly uniform donor layer. Recent advances in single ion implementation techniques may also help optimizing donor depth distribution. In fact, the problem of inhomogeneous Electric fields were dealt with in this manner in Ref. [6], which successfully measured the Stark shifted hyperfine interaction between the donor electronic and nuclear spins. Simulations of the ion implementation process can also yield an estimate of the typical

uncertainty in donor depths, which can be incorporated in the data analysis. In principle STM fabrication techniques could provide more precise donor placement [22].

In addition, clever gate designs can be utilized that combine the advantages of fairy uniform Electric fields generated form a parallel plate capacitor-lie structure. A possible problem could be excessive shielding of the microwave radiation, preventing proper detection of the spin excitation. To eradicate this problem, an inter-digitated gate structure was used in Ref [6]. The field generated by this structure was parallel to the surface and was uniform to a good degree at greater depths. This distribution can be used to take an ensemble average of the signal to relate it to the spin excitation. Also, we have considered the expected electric field distribution of the device in our analysis. Reasonable uncertainty is incorporated in the Electric field to predict suitable field regimes for measurements. All these measurements will help mitigate the effect of inhomogeneous fields.

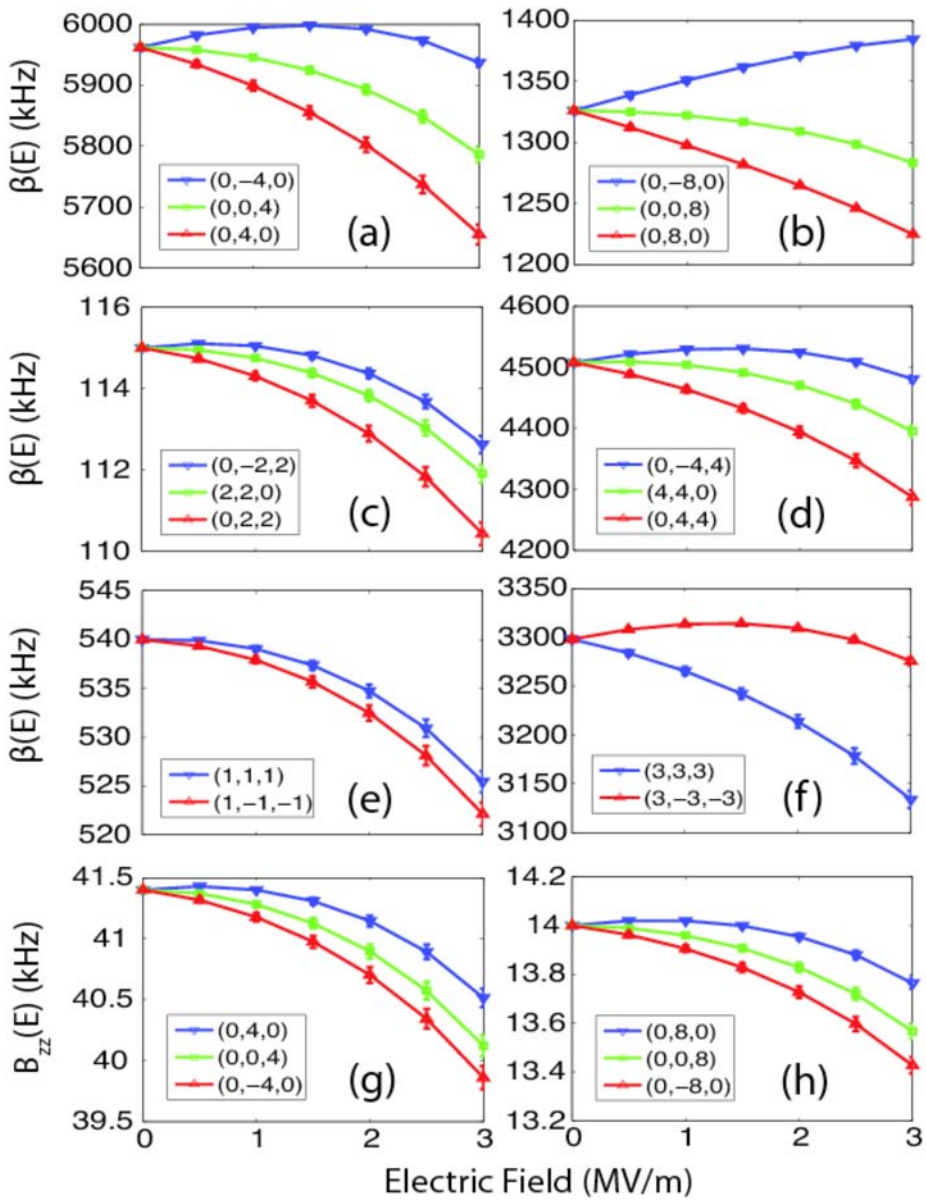

Figure 3.2 Relative change in the contact hyperfine coupling β as a function of electric field for two groups (shells) of points along <100> (a, b), {110} (c, d), and <111> (e, f). The coordinates of the lattice sites are in units of $a_0/4$, where a_0=0.543095 nm. Stark shift of a dipolar component B_{zz} is also shown in (g) and (h) for two shells. The error bars correspond to an estimated uncertainty of 0.1 MV/m in the electric filed. The $\alpha(0)$ values have been taken from Refs [25, 29].

3.4.3 Calculation of Hyperfine and Anisotropic Hyperfine frequency peak

In Figure 3.2, we show the contact hyperfine frequencies as a function of electric field for 6 different groups (shells) of sites around the donor. Fig 3.2a and 3.2b are for sites along [100] with distances of a_0 and $2a_0$ from the donor respectively. The degenerate point at E=0 splits into three curves for these groups, as discussed before. Fig 3.2c and 3.2d are for two shells along [111]. The 12 equivalent points in a shell of [110] split into 3 groups, while the 4 equivalent points of a shell of [111] split into two groups.

As shown in Figure 3.2, the frequency axes of the various plots do not overlap with each other with each other even at fields of 3 MV/m. This means that the shells can be distinguished even in the presence of electric fields. To show the detectability of the points within a shell, we have incorporated an uncertainty of 0.1 MV/m (estimated from Figure 1 of Ref [6]) in the electric field, and represented by error bars in Figure 3.2. This shows that even with some inhomogeneity in the field, most sites can still be identified. Furthermore, the distinguishable due its small splitting and low resonance frequencies. A measurement of the shift of the contact hyperfine frequencies directly provides a measure of the shift in the electron probability density as $\beta(E) - \beta(0) \propto |\psi(E)|^2 - |\psi(0)|^2$.

In Fig 3.2g and 3.2h, we show the Stark shift of one of the dipolar components B_{zz}. These terms are considerably small in magnitude relative to B_{zz}. These terms are considerably small in magnitude of the field-induced deformation in the wave function about the donor nucleus through the dipole operator (eq (1)). Theoretical models involving donor potential and crystal band-structure may be optimized to fit these hyperfine components, and thus to improve their accuracy.

Table 3.1 Quadratic (η_2) and linear (η_1) Stark coefficients for the tensor components of 6 shells around the donor in units of $10^{-3} m^2 / MV^2$ for η_2 and $10^{-3} m / MV$ for η_1.

			β		B_{xx}		B_{yy}		B_{zz}		B_{xy}		B_{xz}		B_{yz}	
Class	Shell	Set	η_2	η_1	η_2	η_1	η_2	η_1	η_2	η_1	η_2	η_1	η_2	η_1	η_2	η_1
<0 0 1>	1	(0 0 4)	-3.8	1.7	-3.3	1.6	-4.6	1.9	-3.9	1.8	-3.9	1.8	-0.008	0.6	-0.01	1.4
		(0 4 0)	-3.5	-6.4	-3.3	4.5	-3.8	4.5	-3.8	4.5	-	-	-3.8	4.0	-	-
		$(0\ \bar{4}\ 0)$	-3.6	9.8	-3.7	-1.0	-3.7	-1.0	-3.7	-1.0	-	-	-	-	-	-
	2	(0 0 8)	-4.1	1.8	-2.8	1.5	-5.1	2.1	-3.9	1.8	-4.5	1.9	-0.004	0.5	-0.006	1.6
		(0 8 0)	-2.2	18.7	-3.7	5.8	-3.8	5.8	-3.7	5.8	-	-	-2.9	-0.27	-	-
		$(0\ \bar{8}\ 0)$	-2.2	21.5	-3.7	-2.4	-3.7	-2.4	-3.7	-2.4	-6.0	1.6	-2.8	5.5	-	-
<1 1 0>	1	(0 2 2)	-3.8	-1.5	-3.6	2.8	-2.9	7.4	-4.3	-1.8	-3.8	-0.1	-4.0	3.1	-3.9	2.2
		$(0\ \bar{2}\ 2)$	-3.9	5.0	-3.6	0.6	-2.7	-4.4	-4.4	5.6	-3.8	3.6	-4.0	0.5	-3.9	1.3
		(2 0 2)	-3.6	2.2	-4.4	2.0	-4.4	2.0	-4.4	2.0	-3.8	4.7	-3.9	2.6	-3.8	4.7
	2	(0 4 4)	-3.5	-5.7	-3.5	4.0	-3.4	17.7	-3.6	-9.7	-3.1	-4.9	-4.3	5.0	-3.9	2.9
		$(0\ \bar{4}\ 4)$	-3.6	9.1	-3.4	0.7	-3.0	14.5	-3.8	13.1	-3.1	8.0	-4.4	1.3	-3.9	0.6
		(4 0 4)	-3.9	3.8	-4.7	3.2	-4.7	3.2	-4.7	3.2	-4.4	26.4	-3.7	3.7	-4.4	26.4
<1 1 1>	1	$(\bar{1}\ \bar{1}\ \bar{1})$	-3.8	2.8	-0.1	0.4	0.3	-0.8	-0.1	0.4	-3.9	1.2	-3.8	1.3	-3.9	1.2
		$(1\ 1\ \bar{1})$	-3.8	0.7	-0.1	-0.3	0.3	0.6	-0.1	-0.3	-3.9	2.4	-3.8	2.2	-3.9	2.4
	2	(3 3 3)	-3.6	-5.6	-0.04	-0.7	0.09	1.5	-0.04	-0.7	-4.2	7.4	-3.1	-3.0	-3.9	7.4
		$(3\ \bar{3}\ 3)$	-3.7	9.1	-0.06	0.8	0.1	-1.5	-0.06	0.8	-4.2	-3.7	-2.0	6.1	-3.9	-3.7

We provide quantitative Stark shift data in Table 3.1 for the components β and B $(B_{xx}, B_{yy}, B_{zz}, B_{xy}, B_{xz}, B_{yz})$ of the six shells considered in this work. To concisely present the Stark shifted hyperfine frequencies, we fitted the curves of Figure 3.2 to the form $\Delta\alpha(\vec{E}) = \alpha(0)(\eta_2 E^2 + \eta_1 E)$, where $\alpha = (\beta, B_{ij})$, η_2 and η_1 are the quadratic and the linear Stark coefficients respectively. The values of η_2 and η_1 obtained from the fit are listed in Table 3.1. Given the hyperfine tensor component at E=0 for a shell and an applied field value, one can calculate both the Fermi contact hyperfine coupling and a dipolar tensor component using this table. As an example, the zero-field hyperfine frequencies of β and B_{zz}, reported in Table II of Ref [25] for the first shell along [100], are 2981 and 41.4 kHz respectively. With E = 4 MV/m, using Table 3.1 and the quadratic equation, we predict that β and B_{zz} of the site (0,4,0) decrease by 243 and 3.3 kHz respectively, a net charge which should be experimentally detectable. In comparison, the other two non-equivalent sites, $(0,\bar{4},0)$ and (0,4,0) are shifted by 55 and 160 kHz in β

and 0.7 and 2.2 kHz in B_{zz} respectively. Therefore, these 3 sites should be distinguishable.

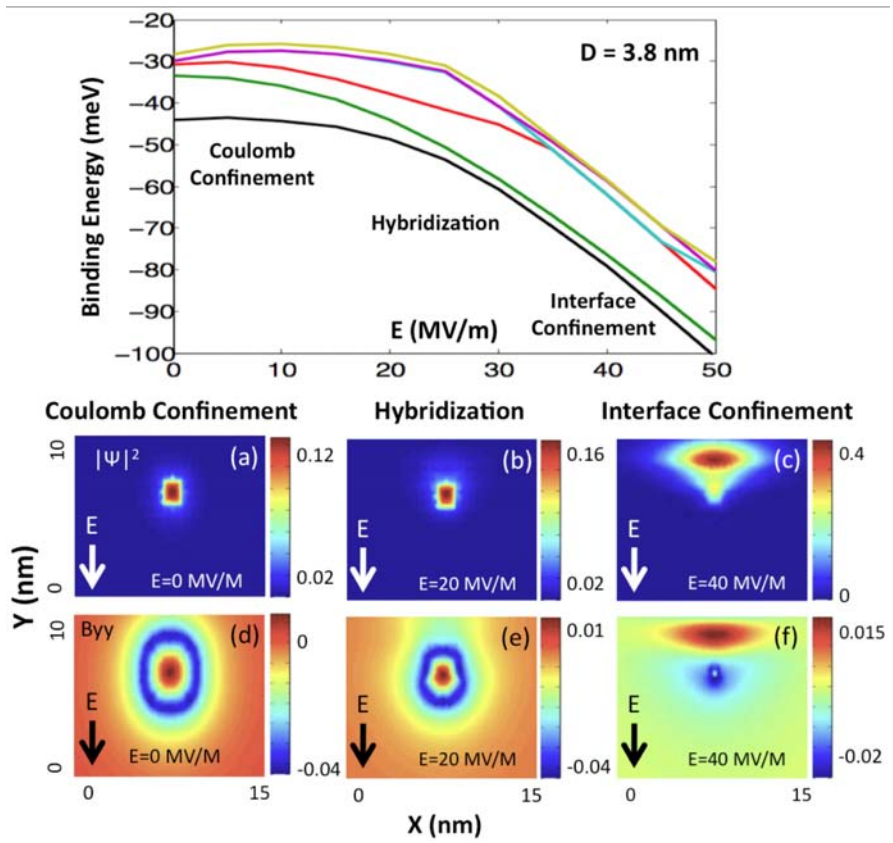

Figure 3.3 Top row: The Stark shifted spectrum of a P donor at 3.8 nm from an oxide interface. Bottom row: (a), (b) and (c) show the P donor ground state wave function at three different electric fields, while (d), (e), and (f) show the corresponding hyperfine maps in the form of B_{yy} tensor component. The electric field is perpendicular to the interface.

Lastly, we give an illustration of how the method is useful for understanding the extent of wave function deformation and quantum confinement of direct relevance to quantum nanoelectronics [13]. Figure 3.3 shows the spectrum and the wave functions of a P donor at 3.8 nm depth from the oxide interface subjected to three different electric fields 0 MV/m, 20 MV/m, and 40 MV/m (Fig 3.3a, 3.3b, and 3.3c respectively). In this regime, the donor wave function can be modified adiabatically by the field [9, 33, 35, 36], as the electron makes a transition from a purely Coulomb confined state at E = 0 MV/m to a purely 2D confined state at the interface at E = 40 MV/m. In the intermediate field regime (E = 20 MV/m), the electron resides in a superposition of Coulomb bound and

surface abound states (Fig 3.3b). This serves an example of controlled wave function engineering by electric fields. An associated dipolar tensor component, B for example, is shown on the 2nd row of Fig 3.3 (d, e, and f), and reflects the gradual symmetry change of the donor wave function.

3.5 Conclusion

In conclusion, we proposed hyperfine maps of donor wave functions as a means of experimentally characterizing field induced distortions and symmetry changes of the real space wave functions. The nuclear spin of a 29 Si atom can essentially act as a probe of the donor wave function, providing a site by site map of the hyperfine interaction to electron localization. Such maps can help us investigate the unknown electronic wave functions in novel Si nanostructures for either quantum computing or nanoelectronic applications. The hyperfine maps can also help to fine tune various modeling techniques, many of which suffer from an inadequate knowledge of atomic scale variations in confining potentials. The predictions of the Stark shift of the hyperfine tensors for six different shells near a P donor indicate that experimental detection of engineered wave functions is feasible for lattice sites in the immediate vicinity of the donor, thus providing a probe of the wave function at sub-Bohr radius resolution.

4. QUANTUM TRANSPORT THROUGH SINGLE DONOR IN A SHORT CHANNEL SEMICONDUCTOR

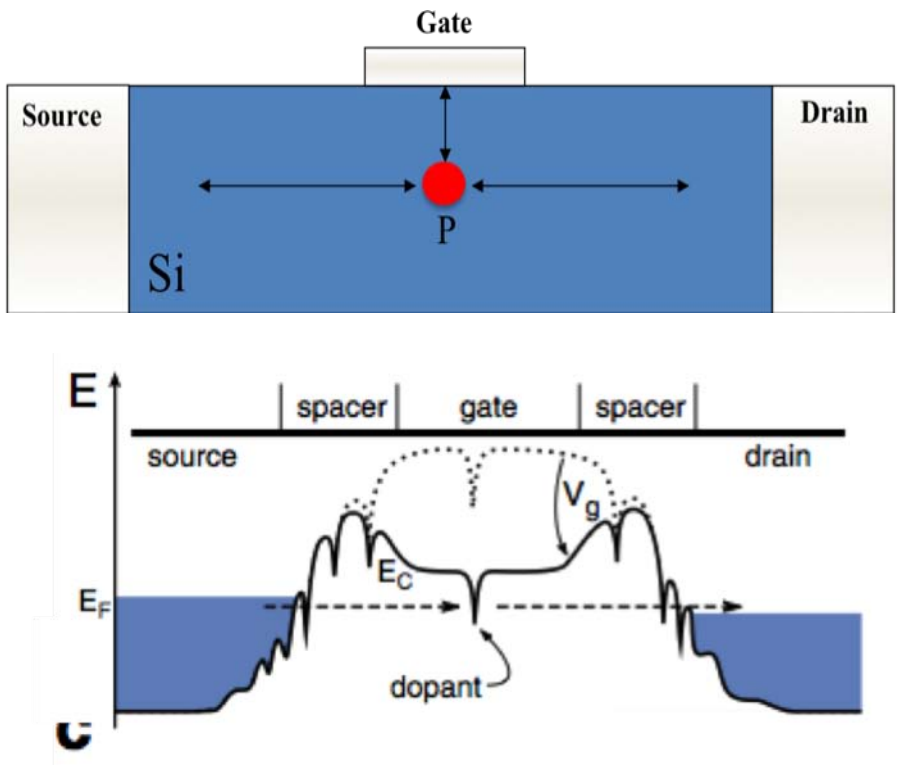

Figure 4.1 Top: The schematic of a short channel semiconductor with single donor Bottom: Conduction band profile with attracting Coulomb potential of isolated dopants for an applied gate voltage corresponding to resonant tunneling through a single dopant in the channel. (Fig2 of Ref. [37])

More understanding of quantum transport with single dopant in a short channel of a semiconductor will lead us to dopant based quantum devices. Since phosphorus impurities have identical electrostatically, it can replace quantum dots in applications such as nanoscale metal oxide semiconductor field effect transistors (MOSFETs) and quantum dot based quantum computing models.

In this study we are going to investigate the effect of the single donor in the nonequilibrium electronic state by controlling quantum transport characteristics. Single donor spin can be considered as a qubit information in quantum computing models, and this transport through a donor will give us an idea of transport of qubit information with understanding of high precision control of single qubit.

Semi-empirical tight-binding method based tools (NEMO 3-D and OMEN) will be used to treat this problem in the atomistic level. Self-consistent field calculation will be employed with varying parameters such as channel length, temperature and donor depth. We are going to show the charging effect of the localized electrons in ion of a short channel semiconductor by calculating various results such as single donor IV characteristics, electron density in the device, energy spectrum of the screening charge in the donor, and conductance.

LIST OF REFERENCES

LIST OF REFERENCES

[1] B. E. Kane, "A silicon-based nuclear spin quantum computer," Nature, 393, 133 (1998).

[2] R. Vrijen, Eli Yablonovitch, K. Wang, H. W. Jiang, A. Balandin, V. Roychowdhury, T. Mor, and D. Divincenzo, "Electron-spin-resonance transistors for quantum computing in silicon-germanium heterostructures," Physics Review A, 62, 012306 (2000).

[3] Igor Zutic, Jaroslav Fabian, S. Das Sarma, "Spintronics: Fundamentals and applications," Reviews of Modern Physics, 76, 323 (2004).

[4] Frank J. Ruess, W. Pok, K. E. J Goh, Alex R Hamilton, and Michelle Y Simmons, "Electronic properties of atomically abrupt tunnel junctions in silicon," Physics Review B, 75, 121303 (2007).

[5] Frank J. Ruess, Bent Weber, Kuan Eng J Goh, Oleh Klochan, Alex R Hamilton, and Michelle Y Simmons, "One-dimensional conduction properties of highly phosphorus-doped planar nanowires patterned by scanning probe microscopy," Physics Review B, 76, 085403 (2007).

[6] F. R. Bradbury, A. M. Tyryshkin, G. Sabouret, J. Bokor, T. Schenkel, and S. A. Lyon, "Stark Tuning of Donor Electron Spins in Silicon," Physics Review Letter, 97, 176404 (2006).

[7] L. C. L. Hollenberg, A. S. Dzurak, C. Wellard, A. R. Hamilton, D. J. Reilly, G. J. Milburn, and R. G. Clark, "Charge-based quantum computing using single donors in semiconductors," Physics Review B, 69, 113301 (2004).

[8] L. C. L. Hollenberg, A. D. Greentree, A. G. Fowler, and C. J. Wellard, "Two-dimensional architectures for donor-based quantum computing," Physics Review B, 74, 045311 (2006).

[9] M. J. Calderon, B. Koliller, X. Hu, and S. Das Sarma, "Quantum Control of Donor Electrons at the Si-SiO_2 Interface," Physics Review Letter, 96, 096802 (2006).

[10] D. Loss and D. P. Vincenzo, "Quantum computation with quantum dots," Physics Review A, 57, 120 (1998).

[11] Srijit Goswami, K. A Slinker, Mark Friesen, L. M Mcguire, J. L Truitt, Charles Tahan, L. J Klein, J. O Chu, P. M Mooney, Daniel W Van Der Weide, Robert Joynt, S. N Coppersmith, and Mark A Eriksson, "Controllable valley splitting in silicon quantum devices," Nature Physics, 3, 41 (2007).

[12] G. Klimeck, F. Oyafuso, T. B. Boykin, R. C. Bowen, and P. V. Allmen, "Development of a Nanoelectronic 3-D (NEMO 3-D) Simulator for Multimillion Atom Simulations and Its Application to Alloyed Quantum Dots," Computer Modeling in Engineering and Science (CMES) Volume 3, No. 5 pp 601-642 (2002), ISSN: 1526-1492., G. Klimeck, S. Ahmed, N. Kharche, M. Korkusinski, M. Usman, M. Prada, and T. Boykin, "Atomistic Simulation of Realistically Sized Nanodevices Using NEMO 3-D: Part II - Applications," IEEE Transaction Electron Device, 54, 2079, (2007).

[13] G. P. Lansbergen, R. Rahman, C. J. Wellard, I. Woo, J. Caro, N. Collaert, S. Biesemans, G. Klimeck, L. C. L. Hollenberg, and S. Rogge, "Gate-induced quantum-confinement transition of a single dopant atom in a silicon FinFET," Nature Physics, 4, 656 (2008).

[14] W. Kohn and J. M. Luttinger, 'Theory of Donor States in Si', Physics Review B, 97, 897 (1955).

[15] J. M. Luttinger and W. Kohn, 'Motion of Electrons and Holes in Perturbed Periodic Fields', Physics Review, 97, 869 (1955).

[16] Rajib Rahman, Cameron J. Wellard, Forrest R. Bradbury, Marta Prada, Jared H. Cole, Gerhard Klimeck, and L. C. L. Hollenberg, "High precision quantum control of single donor spins in Si," Physics Review Letter, 99, 036403 (2007).

[17] Rajib Rahman, Seung H. Park, Jared H. Cole, Andrew D. Greentree, Richard P. Muller, Gerhard Klimeck, and Lloyd C. L. Hollenberg, "Atomistic simulations of adiabatic coherent electron transport in triple donor systems", Physics Review B Vol. 80, 035302 (2009).

[18] Rajib Rahman, Seung H. Park, Timothy B. Boykin, Gerhard Klimeck, Sven Rogge, Lloyd C. L. Hollenberg, "Gate induced g-factor control and dimensional transition for donors in multi-valley semiconductors", Physics Review B Vol.80 134935 (2009).

[19] Rajib Rahman, Seung H. Park, Gerhard Klimeck, Lloyd C. L. Hollenberg, "Stark tuning of the charge states of a two-donor molecule in silicon", arXiv:0907.3929 (2009).

[20] Seung H. Park, Rajib Rahman, Gehard Klimeck, Lloyd C. L. Hollenberg, "Mapping donor electron wave function deformations at sub-Bohr orbit resolution", Physics Review Letter, (2009).

[21] D. K. Wilson and G. Feher, 'Electron Spin Resonance Experiments on Donors in Silicon. III. Investigation of Excited States by the Application of Uniaxial Stress and Their Importance in Relaxation Processes', Physics Review, 124, 1068 (1961).

[22] S. R. Schofield, N. J. Curson, M. Y. Simmons, F. J. Ruess, T. Hallam, L. Oberbeck, and R. G. Clark, "Atomically Precise Placement of Single Dopants in Si," Physics Review Letter, 91, 136104 (2003).

[23] D. N. Jamieson, C. Yang, T. Hopf, S. M. Hearne, C. I. Pakes, S. Prawer, M. Mitic, E. Gauja, S. E. Andresen, F. E. Hudson, A. S. Dzurak, and R. G. Clark, "Controlled shallow single-ion implantation in silicon using an active substrate for sub-20-keV ions," Applied Physcis Letter, 86, 202101 (2005).

[24] S. E. S. Andresen, R. Brenner, C. J. Wellard, C. Yang, T. Hopf, C. C. Escott, R. G. Clark, A. S. Dzurak, D. N. Jamieson, and L. C. L. Hollenberg, "Charge State Control and Relaxation in an Atomically Doped Silicon Device," Nano Letter, 7, 2000 (2007).

[25] Edward B. Hale and Robert Lee Mieher, "Shallow Donor Electrons in Silicon. I. Hyperfine Interactions from ENDOR Measurements," Physics Review, 184, 739 (1969).

[26] G. Feher, "Electron Spin Resonance Experiments on Donors in Silicon. I. Electronic Structure of Donors by the Electron Nuclear Double Resonance Technique," Physics Review, 114, 1219 (1959).

[27] Edward B. Hale and Robert Lee Mieher, "Calculation of Anisotropic Hyperfine Constants for Lattice Nuclei near a Shallow Donor*," Physics Review B, 3, 1955 (1971).

[28] Jerry L. Ivey and Robert Lee Mieher, "Ground-state wave function for shallow-donor electrons in silicon. II. Anisotropic electron-nuclear-double-resonance hyperfine interactions," Physics Review Letter, 29, 176 (1972).

[29] H. Overhof and U. Gerstmann, "Ab Initio Calculation of Hyperfine and Superhyperfine Interactions for Shallow Donors in Semiconductors," Physics Review Letter, 92, 087602 (2004).

[30] Edward B. Hale and Theodore G. Castner, Jr., "Ground-State Wave Function of Shallow Donors in Uniaxially Stressed Silicon," Physics Review B, 1, 4763 (1970).

[31] W. M. Witzel, Xuedong Hu, and S. Das Sarma, "Decoherence induced by anisotropic hyperfine interaction in Si spin qubits," Physics Review B, 76, 035212 (2007).

[32] A. Debernardi, A. Baldereschi, and M. Fanciulli, "Computation of the Stark effect in P impurity states in silicon," Physics Review B, 74, 035202 (2006).

[33] C. J. Wellard and L. Hollenberg, "Donor electron wave functions for phosphorus in silicon: Beyond effective-mass theory," Physics Review B, 72, 085202 (2005).

[34] T. Schenkel, J. A. Liddle, A. Persaud, A. M. Tyryshkin, S. A. Lyon, R. de Sousa, and K. B. Whaley, "Electrical activation and electron spin coherence of ultralow dose antimony implants in silicon," Applied Physics Letters, 88, 112101 (2006).

[35] A. S. Martins, R. B. Capaz, and Belita Koiller, "Electric-field control and adiabatic evolution of shallow donor impurities in silicon," Physics Review B, 69, 085320 (2004).

[36] G. D. J. Smit, S. Rogge, J. Caro, and T. M. Klapwijk, "Stark effect in shallow impurities in Si," Physics Review B, 70, 035206 (2004).

[37] H. Sellier, G. P. Lansbergen, J. Caro, and S. Rogge, "Transport Spectroscopy of a Single Dopant in a Gated Silicon Nanowire", Physics Review Letters, 97, 206805 (2006)

APPENDICES

A. CONCEPT OF SHELL

Concept of shell is required to describe everything in terms of physical locations of lattice sites. The concept of "shells" is quite common in ESR literature and it is difficult to describe correlations between lattice sites and spin excitations without this concept. Basically we grouped all the zincblende lattice sites into shell 1 and shell 2 in all classes rather than conventional concept of shell for better understanding. We denoted lattice coordinates with three integer coordinates (n1, n2, n3) with figures of each direction of shell. All lattice sites can be grouped into classes.

[001] axis Class :

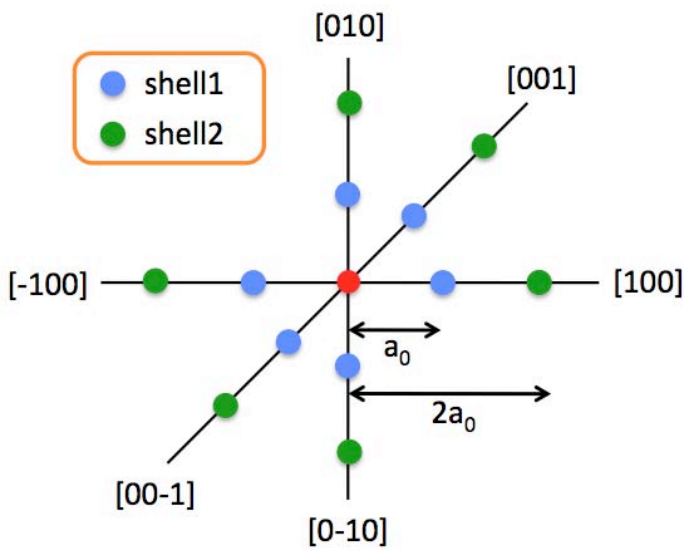

Figure A.1 shells of the [001] axis clas

There are 6 sites per shell in the [001] axis class. Shell1 is a0 away from single donor nuclear, and shell 2 is 2a0 away from single donor.

[110] axis Class :

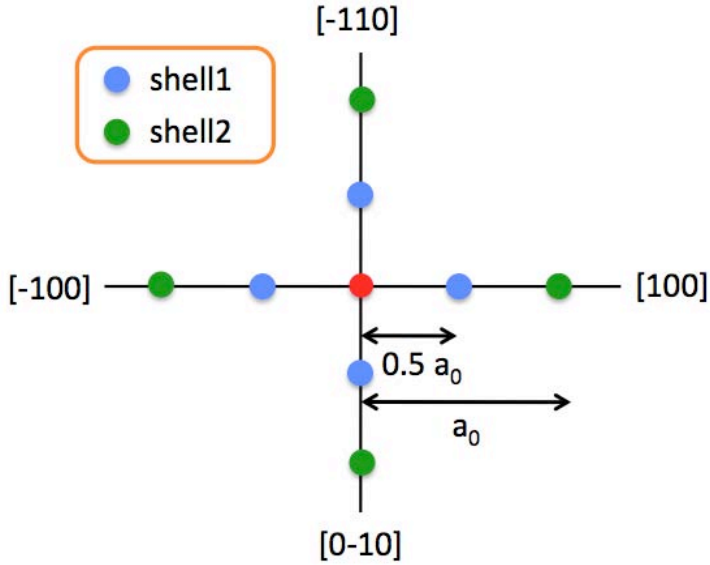

Figure A.2 xy plane of (110) plane class

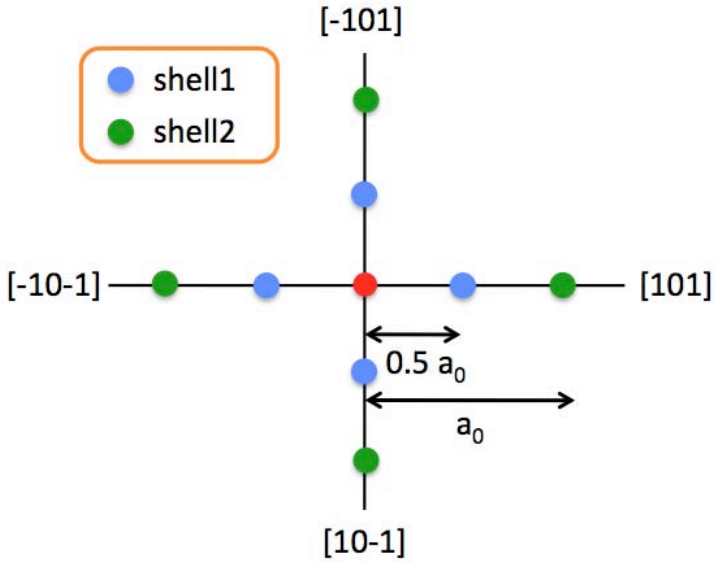

Figure A.3 xz plane of (110) plane class

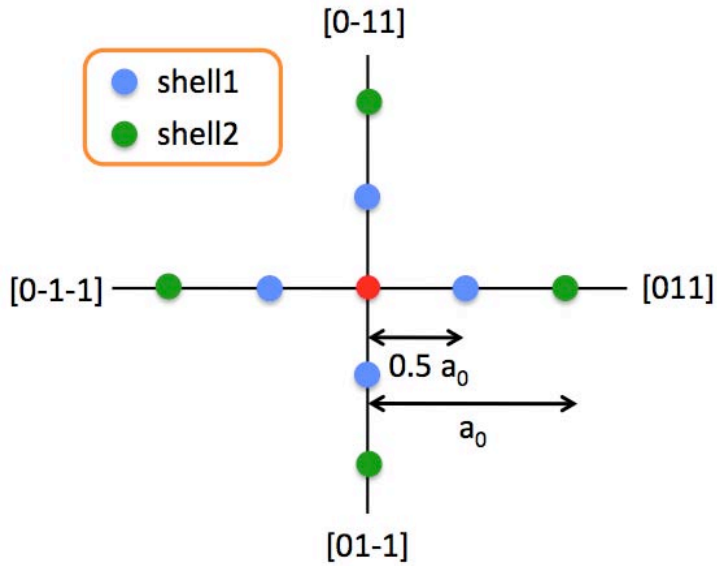

Figure A.4 yz plane of (110) plane class

The three planes are placed orthogonal to each other to visualize the 3D picture. Therefore, there are 12 sites per shell in (110) plane class.

[111] axis Class :

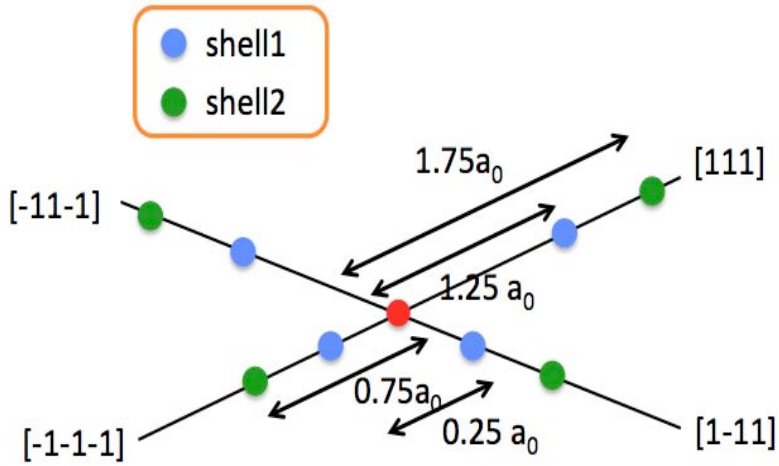

Figure A.5 Atom locations on two lines joining 4 corners of a cube.

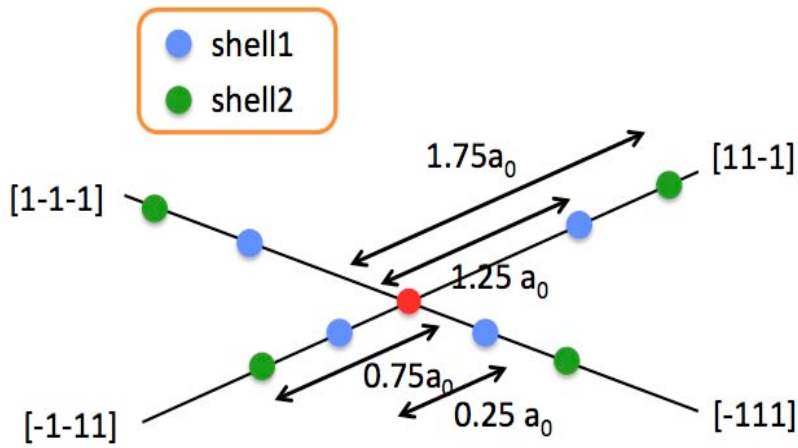

Figure A.6 Atom locations on other two lines joining 4 corners of a cube.

These two planes are placed orthogonal to each other to visualize the 3D picture. Therefore, there are 4 sites per shell in [111] axis class.

B. REFERENCE OF HYPERFINE FREQUENCY CALCULATION

In calculation of hyperfine frequencies, we fitted the curves of figure 3.2 'Relative change in the contact hyperfine coupling' to the form $\Delta\alpha(\vec{E}) = \alpha(0)(\eta_2 E^2 + \eta_1 E)$, where $\alpha = (\beta, B_{ij})$, η_2 and η_1 are the quadratic and the linear Stark coefficients respectively. The values of η_2 and η_1 obtained from the fit are listed in Table 1. We couldn't include $\alpha(0)$ into the calculation, and the $\alpha(0)$ values for each lattice points have been taken from the tables of references. The tables for $\alpha(0)$ are attached below.

Table B.1 Isotropic hyperfine and modulus the super hyperfine interactions (in MHz) for group V donors in Si. The α(0) value for (2,2,0) has taken from 'This work' column of the above table.
'Ab Initio Caculation of Hyperfine and Superhyperfine Interactions for Shallow Donors in Semiconductors.' H. Overhof et al, PRL, 92, 087602 (2004)

Shell		Donor	Exp.	This work	IM	EMT
Donor	(0, 0, 0)	^{31}P	117.53	121.4	71.2	448.0
		^{75}As	198.35	198.6	120.0	850.0
		^{121}Sb	186.80	66.8	89.4	548.0
E	(1, 1, 1)	P	0.540	0.518	0.036	1.524
		As	1.284	1.168	0.006	2.424
		Sb	0.586	2.053	0.090	1.232
	(2, 2, 0)	P	···	0.115	0.608	0.861
			···	0.193	0.788	1.216
		Sb	···	0.587	0.532	0.734
	(1, 1, $\bar{3}$)	P	···	0.053	···	···
		As	···	0.179	···	···
		Sb	···	0.001	···	···
A	(0, 0, 4)	P	5.962	2.963	5.848	8.414
		As	7.720	3.160	7.606	11.400
		Sb	6.202	2.923	5.168	7.324
F	(3, 3, 1)	P	1.680	1.461	1.5776	0.988
		As	2.242	2.351	2.590	1.290
		Sb	1.008	0.848	1.212	0.872

Table B.2 Experimental results for hyperfine tensors in arsenic-, phosphorus-, and antimony-doped silicon. The values are for a positive nuclear g factor. Since 29 Si has a negative g factor, the values should technically be reversed in sign. All values are in kc/sec except angles, which are in degrees. Absolute value signs occur because signs cannot be determined by ENDOR.
'Shallow Donor Electrons in Silicon. I. Hyperfine Interactions from ENDOR Measuremnets', Edward B. Hale and Robert Lee Mieher, Physics Review, 184, 739 (1969)

Shell class	Donor	$\frac{1}{2}a$	B_{zz}	B_{zy}	$\lvert B_{zx}\rvert$	$\frac{1}{2}b_1$	$\frac{1}{2}b_2$	$\lvert\alpha\rvert$	B_{zz}'	B_{yy}'	B_{xx}'
A ⟨001⟩ axis	As	3860	57.0	$\lvert 55.8\rvert$		18.6	23.6		57.0	−84.2	27.2
	P	2981	41.4	$\lvert 41.4\rvert$	0ᵃ	13.8	17.2	0ᵃ	41.4	−62.0	20.6
	Sb	3101	46.0	$\lvert 34.2\rvert$		11.4	17.2		46.0	−57.2	11.2
B {110} plane	As	3000	−41.6	148.2	72.2	−7.4	48.9	67.9	210.4	−83.0	−127.2
	P	2254	−34.0	106.2	39.8	−6.2	32.2	72.2	141.2	−52.0	−89.2
	Sb	1833	−28.6	79.2	20.2	−5.0	22.5	77.5	100.0	−35.0	−65.0
C ⟨111⟩ axis	As	2037		5.8	B_{zy}		2.9		11.6	$-\frac{1}{2}B_{zz}'$	B_{yy}'
	P	1649	0ᵃ	5.0	B_{zy}	0ᵃ	2.5	$54\frac{3}{4}$ᵃ	10.0	$-\frac{1}{2}B_{zz}'$	B_{yy}'
	Sb	1397		6.0	B_{zy}		3.0		11.8	$-\frac{1}{2}B_{zz}'$	B_{yy}'
D {110} plane	As	1292	4.2	20.4	25.4	0.4	12.2	50.6	47.8	−25.2	−22.6
	P	1117	3.6	16.6	22.2	0.7	10.6	50.1	41.0	−22.8	−18.4
	Sb	1003	0.0	17.4	17.4	0.0	8.7	54.6	34.8	−17.4	−17.6
E ⟨111⟩ axis	As	642		1258	B_{zy}		629		2516	$-\frac{1}{2}B_{zz}'$	B_{yy}'
	P	270	0ᵃ	700	B_{zy}	0ᵃ	350	$54\frac{3}{4}$ᵃ	1400	$-\frac{1}{2}B_{zz}'$	B_{yy}'
	Sb	293		522	B_{zy}		261		1044	$-\frac{1}{2}B_{zz}'$	B_{yy}'
F {110} plane	As	1121	151.0	−41.2	4.6	13.8	44.7	1.4	151.2	−116.8	−34.4
	P	840	116.4	−28.2	11.8	9.6	34.2	4.7	117.6	−87.8	−29.8
	Sb	Not present with $\frac{1}{2}a$>305 kc/sec.									
G {110} plane	As	806	7.0	−1.0	5.6	1.0	3.3	27.1	11.2	−8.6	−2.6
	P	764	5.0	−1.2	5.0	1.1	2.8	29.0	9.0	−7.8	−1.2
	Sb	761	4.6	−1.2	5.2	1.1	2.8	30.7	8.8	−7.8	−1.2
H ⟨111⟩ axis	As	801		62.4	B_{zy}		31.2		124.8	$-\frac{1}{2}B_{zz}'$	B_{yy}'
	P	689	0ᵃ	50.6	B_{zy}	0ᵃ	25.3	$54\frac{3}{4}$ᵃ	101.4	$-\frac{1}{2}B_{zz}'$	B_{yy}'
	Sb	703		44.6	B_{zy}		22.3		89.2	$-\frac{1}{2}B_{zz}'$	B_{yy}'
I {110} plane	As	718	−20.4	31.8	12.0	0.5	11.8	75.5	46.2	−24.6	−21.8
	P	685	−17.4	27.8	13.8	0.8	11.1	72.1	42.8	−23.8	−19.2
	Sb	643	−14.0	22.6	14.4	1.1	9.9	68.5	37.6	−22.0	−15.6
J ⟨111⟩ axis	As	694		6	B_{zy}		3		12	$-\frac{1}{2}B_{zz}'$	B_{yy}'
	P	739	0ᵃ	5.4	B_{zy}	0ᵃ	2.7	$54\frac{3}{4}$ᵃ	10.8	$-\frac{1}{2}B_{zz}'$	B_{yy}'
	Sb	Not found									
K ⟨001⟩ axis	As	758	16.0	$\lvert 7.6\rvert$		2.5	5.3		16.0	−15.6	−0.4
	P	663	14	$<\lvert 12.0\rvert$	0ᵃ	...	...	0ᵃ	...	...	...
	Sb	Not found									
L {110} plane	As	741	−14.6	9.8	8.2	2.6	6.5	72.0	20.8	−18.2	−2.6
	P	582	−11.2	2.6	7.6	3.2	4.8	66.3	13.0	−16.0	3.0
	Sb	425	−5.8	3.8	4.4	1.3	3.0	67.2	9.6	−8.4	−0.8
M {110} plane	As	777	−60.8	65.2	41.4	7.9	32.8	71.6	115.0	−80.0	−35.0
	P	612	−40.6	49.6	35.6	5.2	25.0	68.8	89.4	−60.2	−29.2
	Sb	559	−37.2	44.0	30.6	4.7	22.0	69.5	78.8	−53.4	−25.4
N ⟨111⟩ axis	As	607		4.2	B_{zy}		2.1		8.6	$-\frac{1}{2}B_{zz}'$	B_{yy}'
	P	612	0ᵃ	3.4	B_{zy}	0ᵃ	1.7	$54\frac{3}{4}$ᵃ	6.6	$-\frac{1}{2}B_{zz}'$	B_{yy}'
	Sb	Not found									
O ⟨111⟩ axis	As	739		35.8	B_{zy}		17.9		71.6	$-\frac{1}{2}B_{zz}'$	B_{yy}'
	P	598	0ᵃ	32.6	B_{zy}	0ᵃ	16.3	$54\frac{3}{4}$ᵃ	65.2	$-\frac{1}{2}B_{zz}'$	B_{yy}'
	Sb	670		31.4	B_{zy}		15.7		62.6	$-\frac{1}{2}B_{zz}'$	B_{yy}'
P {110} plane	As	696	−4.8	4.0	4.2	1.6	2.7	67°	8.8	−7.4	−1.5
	P	662	−6	<6	<6	...	...	...	...	...	...
	Sb	629	...	...	...	<4	<4	...	...	...	...
Q {110} plane	As	566	−48.0	101.6	27.6	−3.6	31.7	77.9	134.0	−56.2	−77.6
	P	524	−40.2	84.0	22.8	−2.8	26.4	77.9	111.0	−47.2	−64.0
	Sb	387	−36.0	78.6	31.6	−1.9	26.7	73.0	110.4	−49.6	−60.8
R {110} plane	As	428	24.8	0.0	25.0	3.6	13.4	31.2	46.2	−33.8	−12.4
	P	379	21.0	0.2	19.4	2.6	10.5	30.1	36.8	−26.0	−10.8
	Sb	332	15.0	−2.8	12.0	2.4	7.1	26.5	23.6	−18.8	−4.8

TABLE II (*continued*)

Shell class	Donor	$\frac{1}{2}a$	B_{zz}	B_{xy}	$\lvert B_{xz}\rvert$	$\frac{1}{2}b_1$	$\frac{1}{2}b_2$	$\lvert\alpha\rvert$	B_{zz}'	B_{yy}'	B_{xx}'
S {110} plane	As	377	−5.4	9.2	0.0	−0.2	2.9	90	12.0	−5.4	−6.4
	P	410	−5.4	7.4	0.0	0.1	2.6	90	10.0	−5.4	−4.8
	Sb	525	−5	<4	<4	...	...	...	...	...	...
T {110} plane	As	364	0.0	4.4	4.4	0.0	2.2	55	8.6	−4.4	−4.4
	P	398	0.0	3.8	4.2	0.1	2.1	54	8.2	−4.4	−3.8
	Sb	Not found									
U {110} plane	As	338	...	...	...	<2	<2	...	...	...	...
	P	383	...	...	...	<2	<2	...	...	...	...
	Sb	Not found									
V {110} plane	As	Not present with $\frac{1}{2}a$>320 kc/sec.									
	P	Not present with $\frac{1}{2}a$>300 kc/sec.									
	Sb	504	37.0	0.2	30.2	3.8	17.0	28.5	60.2	−41.6	−18.6
W {110} plane	As	Not found									
	P	328	...	...	...	<2	<2	...	...	...	...
	Sb	Not found									
X {110} plane	As	242	40	30	...	...	...	...	...	...	...
	P	317	29.4	23.6	32.2	−1.8	15.6	38.7	65.8	−27.6	−38.4
	Sb	437	20.4	19.0	20.8	−2.3	10.0	39.5	44.6	−15.4	−29.2

[a] Determined by symmetry.

The α(0) values have taken from '1/2 a' column of the above table to add it to the calculation of fitting the curves of figure 3.2 'Relative change in the contact hyperfine coupling.'